# TSUNAMI – Hyperspectral Imager for Chlorophyll Detection

Emilio Armas, Jacob Silver, Xander Kin

Dept. of Electrical Engineering and Computer Science, University of Central Florida, Orlando, Florida, 32816-2450

***Abstract* – TSUNAMI is a hyperspectral imager, or imaging spectrometer primarily designed to focus on the detection of chlorophyll in plant matter. Within the visible wavelengths of light, spectral features exist across a continuous spectrum. However, the human eye, as well as standard camera sensors can only resolve three color channels: red, green, and blue. Our imager can resolve this data by diffracting an incoming slit of light and scanning across a scene, creating many images, with each at a specific wavelength. Every pixel thus gets its own unique optical spectrum measured.**

***Index Terms* – Diffractive imaging system, line-shaping optics, microcontroller, power converters, user interface, motorized translation stage**

## I. INTRODUCTION

This project centered around an effort to design and fabricate a line-scanning hyperspectral imager for use within the visible/near-infrared (NIR) wavelengths of light. The instrument is able be able to capture an image across a two-dimensional field of view, simultaneously recording an entire spectra per "pixel". Recording an entire spectra per-pixel is a 3D dataset, and naturally with existing imaging sensors being 2D, there must be a way to compromise one metric to enable collecting these data. The method TSUNAMI uses to achieve this goes by limiting a camera's traditional 2D field-of-view to just a vertical line, and translating the sample below along the other spatial axis to capture a strip-image. A linear incident beam is used, as when it is passed through a diffractive grating, it will form a two-dimensional image on a given plane. This image, rather than containing two traditionally spatial dimensions, now includes only the slit's lateral dimension, with the other now being wavelength. When illuminated onto an image sensor array, this image is now a per-pixel spectral representation of the incident beam into the imager. While the final image cannot be captured simultaneously, with this translating target, a faithful hyperspectral image can be produced, where any selected pixel can have a full spectrum read from it. The entire device is powered via an external AC/DC wall-adapter, hosting an on-board GUI for integrated imaging processing, rendering, and control over all hardware subsystems that run the instrument.

Our primary target is to image the spatial distribution of chlorophyll in plant matter. The concentration of chlorophyll across tissues of a plant (such as a leaf) are a prime indicator for plant health. Being able to image chlorophyll concentration across a particular target directly allows professionals in agriculture, biology and ecology the ability to monitor plant stress and senescence. This can directly improve crop yields.

*Figure 1: TSUNAMI Hyperspectral Imager (March 2026)*

## II. SYSTEM COMPONENTS AND DESIGN

Our system can be broken down into various sub-systems, interfaced electrically, optically, and mechanically. Central to the system operation is our diffractive imaging optics, which enable the splitting

of the wavelength and spatial dimensions to our imaging sensor. Our camera sensor interfaces to our embedded Raspberry Pi 4B single-board computer (SBC), hosting the high-level graphical-user-interface (GUI) and imaging processing/rendering. Our motor, its electronic controller, power supplies, and laser diode driver are all controlled by our central microcontroller (MCU), with power being distributed by its host board. Below is a block diagram illustrating these overall connections:

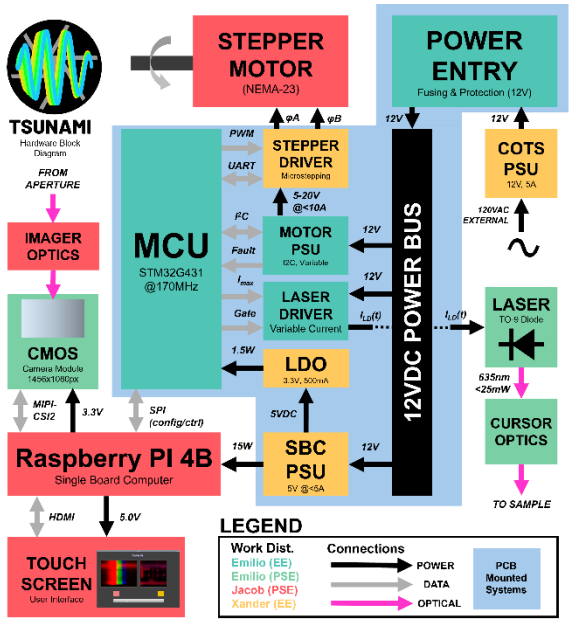


*Figure 2: Overall system hardware block diagram*

### *A. Microcontroller (MCU) Electronics*

The central control of all fundamental hardware was given to an ST-Microelectronics STM32G431 32-bit ARM Cortex-M4 MCU. Our MCU is given the task of managing our hardware elements, being the motor driver, motor power supply, laser diode driver, and interfacing to our SBC for its high-level control. This MCU was chosen for its extensive set of on-board peripherals, such as its integrated 12-bit digital-to-analog converter (DAC) for driving the laser diode current. The STMicroelectronics MCUs feature extensive hardware documentation and a hardware-abstraction-layer (HAL) programming interface from the manufacturer. Firmware was written in C and compiled using the generic *arm-gcc* compiler for the Cortex-M4 CPU, along with the appropriate hardware register header file from the manufacturer.

The MCU, along with the motor driver (addressed later) are hosted on a "hat" style PCB above the Raspberry Pi computer, using its standardized IO connector and mounting points. This board is the MCU/Control board, and was designed on a four-layer FR-4 substrate. This board is also central to distributing and fusing power from its 12V main bus. An 8MHz crystal oscillator, 5V->3.3V LDO, 2.5V reference, debugger connection, and control/reset circuitry are added around the MCU.

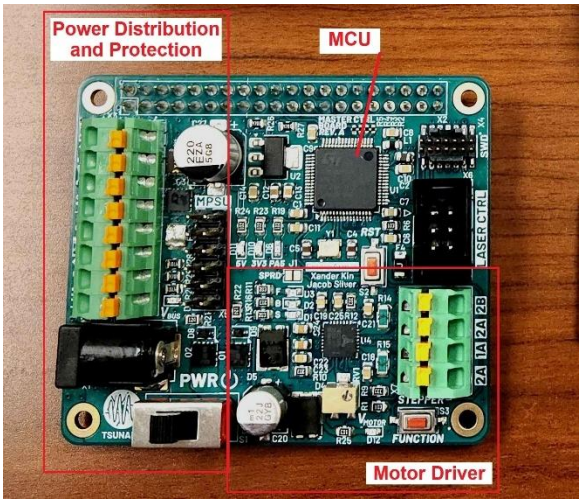


*Figure 3: MCU and Control Board*

### *B. Imager Optics*

The core design consideration of the imager is the axial difference in target data. One axis of detector must record spatial information while the other axis records the first order beam from a diffraction grating. The first main result of this consideration is the need for a slit aperture, as the field-of-view of the wavelength axis must be limited as much as possible to achieve sufficient resolution. In our optics train, this strong vignetting is accomplished by using two slits in the train, as one slit alone still allows for accidental imaging of off-axis rays. Collimation is necessary in order to utilize a diffraction grating accurately.

Collimation is accomplished by an entry two-lens system, with one lens of f = +100 mm and the other with f = -100 mm. Notches in the camera housing allow for movement of the two lens and therefore adjustment of the entry focal length from the scanning design target of 300 mm from the later lens in case translation stage design is changed.

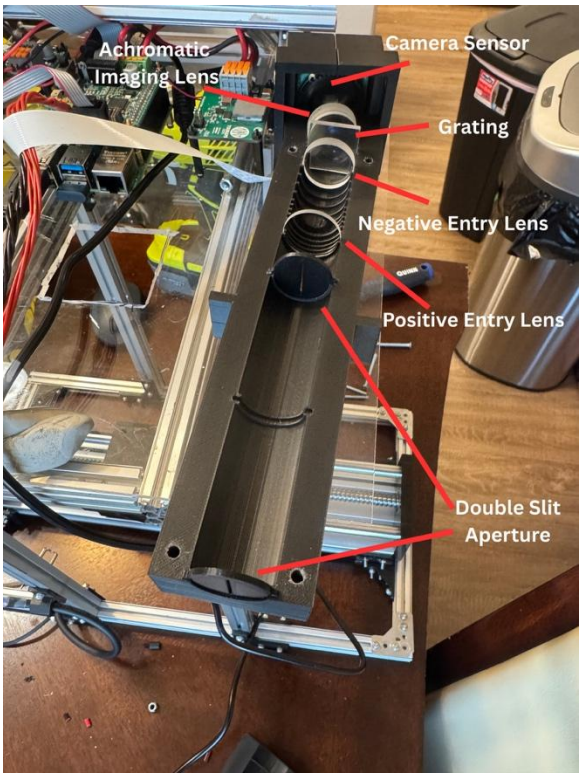


*Figure 4: Implemented optics train, opened for visibility.*

The spatial field-of-view and the wavelength range across the other axis are tied together by the size of the detector. The diffraction angle sets the distance the detector must be from the grating, and the final achromatic imaging lens must have a focal length to match. The angular spread across either axis must be equal, leading to the following calculation:

$$\Delta\theta_{spat} = 2tan^{-1}\left(\frac{h_{det}}{2f_{achr}}\right) \approx \frac{h_{det}}{f_{achr}} \quad (1)$$

$$\Delta\theta_{spec} = sin^{-1}(\rho_{line}\lambda_f) - sin^{-1}(\rho_{line}\lambda_i) \approx \rho_{line}\Delta\lambda \quad (2)$$

$$\Delta\theta_{spat} = \Delta\theta_{spec} \rightarrow f_{achr} = \frac{h_{det}}{\rho_{line}\Delta\lambda} \quad (3)$$

We find that achromat focal length is inversely proportional to both grating line density and wavelength range. We therefore chose the shortest focus achromat (f = 30 mm) and broadest grating (300 lines/mm) readily commercially available which for a detector height of 6 mm gives a wavelength range of 667 nm, just greater than our 550 nm (350 nm – 900 nm) range requirement. With our determined 300 lines/mm grating and a center wavelength of 625 nm, we set an optical axis bend angle of 10.8° to capture the first order beam.

The results of our imager optics tests match our expectations well. Quantitative data is given in our results section. The image below demonstrates the motivation and capability of the system.

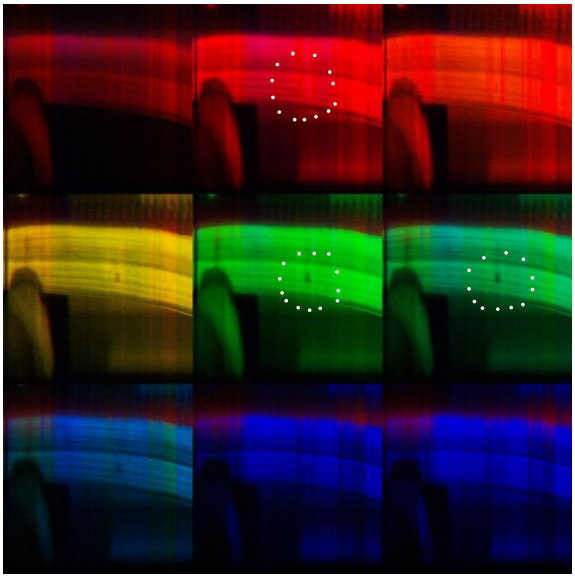

*Figure 5: Captured images of a blade of grass and round leaf from near IR through visible to near UV. The center of a dead spot on the grass is clear in the center and middle right image (white dots circling for clarity). The broader affected zone around the spot is visible in the top middle image.*

### *C. Laser Cursor*

To aid with the user experience of working with the instrument, as well as act as a functionally useful indicator, we found it necessary to design a laser "cursor" subsystem. This is based on a commercially available red laser diode, taking the diode's beam and expanding it along its propagation. The laser will be pulsed in such a fashion where the laser illuminates the target between successive captures along the imagers' translating direction. With human persistence of vision, the imager will be able to display a scan-line as it images. The design of the cursor was a two-front effort between opto-electronic design (laser diode driver), and the optics train to shape our laser diode beam into a diverging line.

The circuitry responsible for the driving of the laser diode follows a custom schematic design, detailed in this section. Our goal with this design was ultimately

to create a voltage to current driving converter, to translate our voltages generated by our DAC peripheral to currents through the diode. A simple single-transistor low-side driver was developed, featuring a single current-feedback amplifier to control the MOSFET transistor. The current-control amplifier's feedback path was designed and tuned to be stable under any large inductance seen in the current sinking path.

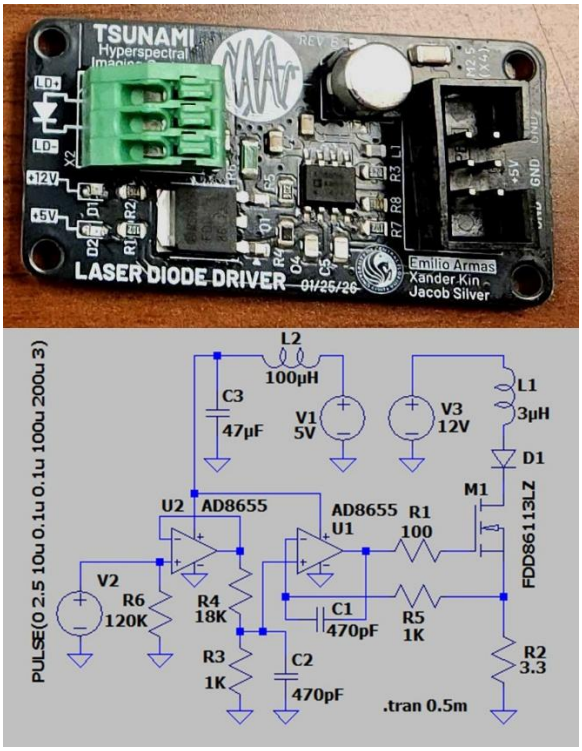


*Figure 6: Schematic and construction of Laser Diode Driver*

The optical design of the line-forming optics needed to immediately address the astigmatic shape of the laser diode's output beam, and carefully shape it into growing line, while remaining simple for cost.

*Figure 7: Laser cursor optics mount (alignment testing)*

The laser diode's beam diverges at 8° along one axis, and 30° from the other, due to the rectangular output facet on the diode's central resonator. Because of this, the first objective of the optics train was to collimate the beam's 8° slow axis, and limit the divergence of the 30° fast axis. From a paraxial approach, the first lens (plano-convex) was inserted after the diode. This immediately collimated the slow axis. From there, a cylindrical lens curved along the fast axis would form a beam expander for that length of the beam. The beam expander was purposely designed to not output a collimated output, and instead diverge at the same 6° angle as our camera FOV. Dimensions between elements were optimized to fit a linear spot with ZEMAX optics studio, after a first pass with paraxial design. Ultimately the cursor was designed to reach a target line shape (FWHM brightness) of 20:1 at its target distance of >300mm.

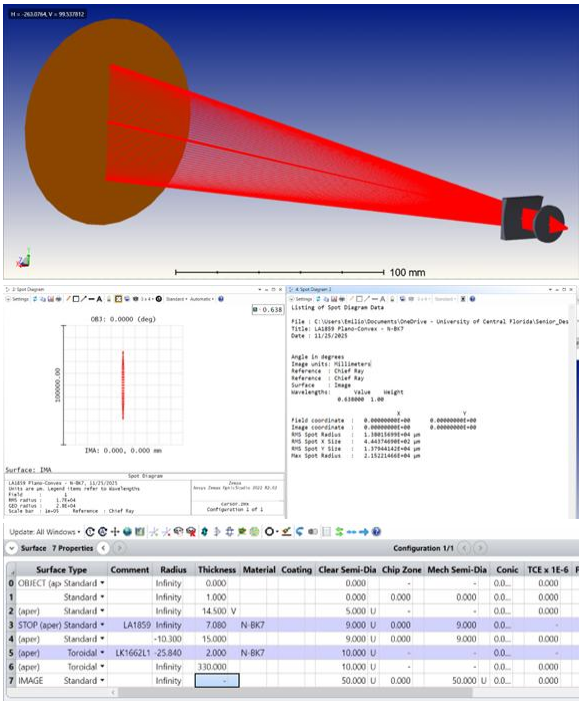


*Figure 8: Laser Cursor 3D render, spot size metrics, and lens-data table*

*D. Translation Stage, Motor, and Chassis*

Our translation stage was purchased as a commercial-off-the-shelf (COTS) assembly. This assembly came complete as a length of aluminum extrusion, motor mount, threaded rod-axle, sliding rod support rails, endplates, and a NEMA-23 stepper motor all mounted. The motor came pre-wired, but this harness was manually extended to allow the motor driver electronics to reach it. The translation stage ultimately stands as the center of the chassis assembly and the bulk of the imager's weight. The chassis was constructed generally from COTS parts for general

aluminum extrusion projects. Extrusion cuts and fastening brackets were bolted together to generally fit the translation stage and support the imager and electronics above it in a gantry.

*E. SBC Power Supply & Motor Driver Power Supply*

Our energy source consists of a DC power jack with an output voltage of 12V and 10A, more than enough for the system we need to power. The Raspberry Pi has highest power consumption with it needing up to 3A of constant operating current, and a 5A peak maximum, meaning around 10W to 20W. Our MCU sits around 330 mW, while our motor driver will take in 10W – 58W only when on.

Our SBC power supply needs tight control since the input of the Raspberry Pi demands a 5V and 5A supply. Using the TPS54541 IC allows us to accept a 9-36V bus input while regulating up to 5A at 5.1V continuously. The 5.1V is to account for cable/connector loss. This will allow enough headroom for potential current spikes and losses of cable for power our Raspberry Pi 4B.

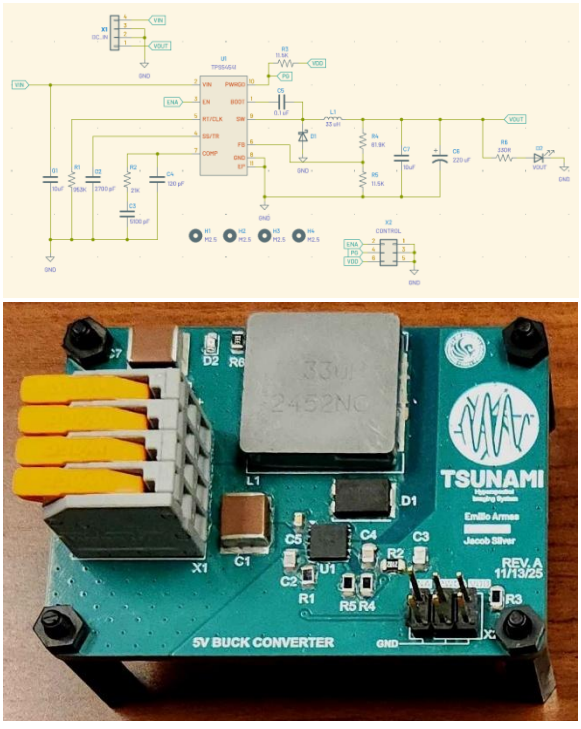


*Figure 9: SBC Power Supply, schematic and assembly*

Here we follow the IC datasheet in creating the layout. We use a four-layer stack-up, bottom and top copper layers for signaling and large copper pours, with the inner layers being solid ground planes for the power circuitry and the analog/control circuitry. We kept the parts at 0805 and provided enough thermal via's for when the board is running for a good amount of time.

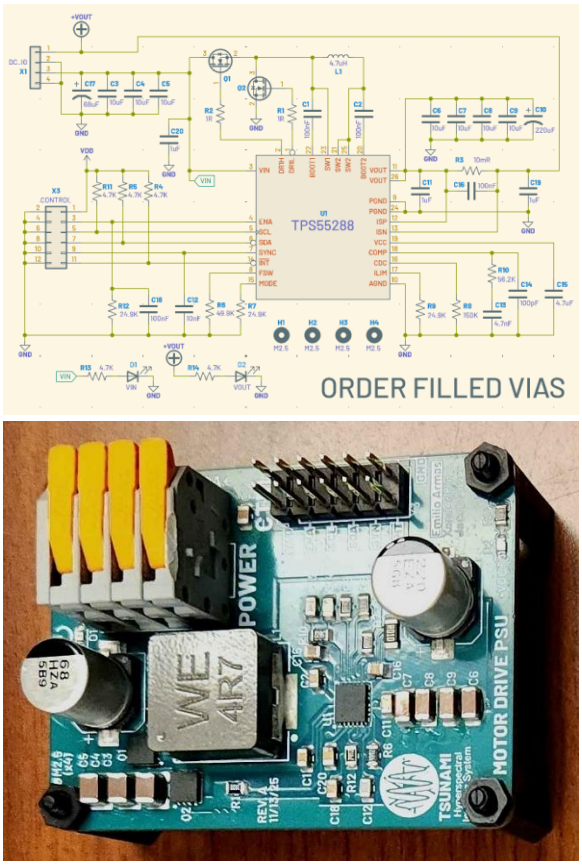


*Figure 10: Motor driver PSU, schematic and assembly*

The motor driver power supply will need to handle higher power when it's on, which the buck/boost topology will be beneficial to use. The motor driver is TSP55288 based, regulating 5-20V up to 3A. Implementing I2C is necessary which we have also implemented to interface with the MCU. The output voltage/current and system status is digitally controlled by the I2C interface to the MCU, which will then be controlled by the user via touchscreen. The variable voltage allows us to control the motor step energy and speed.

A similar approach was followed in creating the motor driver PSU, following the IC datasheet for the components. Top and bottom copper layers are for tracing and signaling all the connections, with the grounding plane for power and analog/control

circuitry. TI mentioned that only connecting the analog ground plane to the power ground on the return area of the VCC decoupling capacitor ensures noisy power signals return to ground with minimal interference.

### *F. Single-board Computer and Control Software*

Our Raspberry Pi is the system module that brings everything together. It provides a UI and user controls to be able to control the camera and take photos at the proper wavelength. It sends these commands by interfacing with our MCU via SPI, with a structured 9-byte command system we have laid out. It also functions as the base of our main PCB containing our MCU, motor driver, and external connections. We also have a touch screen that provides easy user maneuverability with easy-to-understand controls.

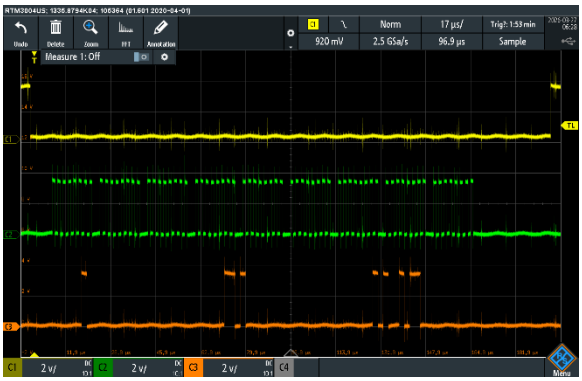

*Figure 11: Waveform captured of a typical SPI transfer from SBC to MCU. Traces: Chip-Select (Yellow), SCLK (Green), MOSI (Orange). This is a forward-translation command for the translation motor.*

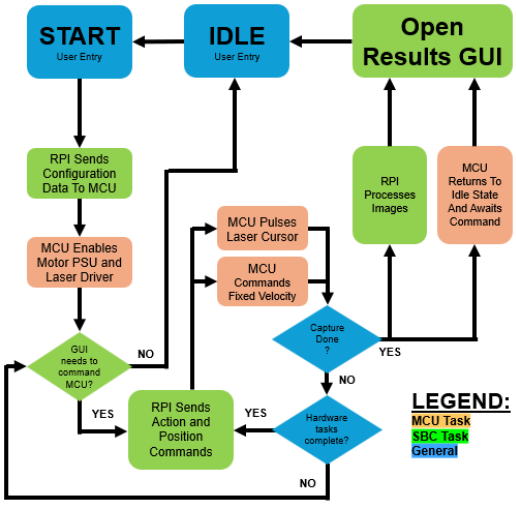


*Figure 12: SBC to MCU general software tasks*

Our command structure between the SBC and MCU consists of a single command number byte, followed by up to eight data bytes for specific arguments in different commands. For example, our forward motor translation command is command #1, the eight data bytes represent two unsigned 32-bit integers for both motor velocity (in µm/sec) and motor scan time (in ms). The MCU receives all high-level commands from the SBC and executes them by running its own subroutines to control our electronics hardware.

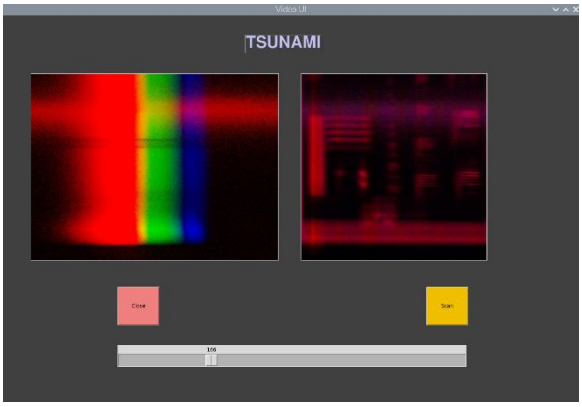


*Figure 13: Current GUI for imaging and monitoring'*

We employ a python-based GUI running on the SBC with touch-screen controls. The screen sits front-and-center, elevated to the top of the overall instrument chassis. Our GUI is based on the Tkinter software framework for python. Subroutines for SPI command data transfers, image saving, camera image acquisition, and other controls are hosted within the GUI. For faster scan times, we are moving towards a faster C script for image acquisition and SPI control to act as a back-end to the GUI we use.

## III. TESTING/RESULTS

### *A. SBC Power Supply Efficiency*

Determining the efficiency of power supply will help us give quantitative evidence that our system will hold up to the standards we need.

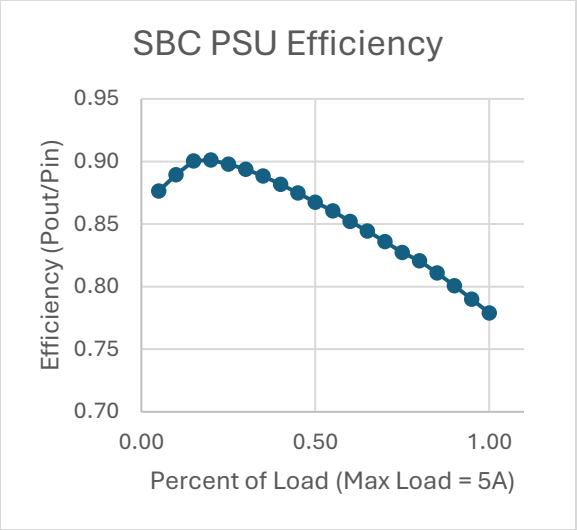


Here is the percentage of load being applied vs the efficiency we gathered. We gathered 20 data points going from 0 A to 5A with an increment of 0.25A. We accounted for cable loss for both input and output for this graph. Our efficiency tends to peak around 20% of our max load but still remains at around 85% efficiency at 60% or 3A which is our constant current consumption. This visualizes the performance of power supply to the Raspberry Pi 4b.

*B. Motor Driver Power Supply Efficiency*

Our motor driver power supply also requires its own separate power supply. This is more quantitative evidence for the standards our system needs.

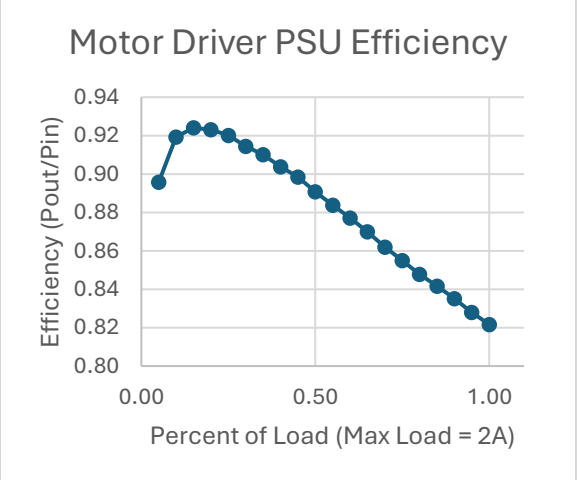


Here, our chart looks similar to the power supply. This also had 20 data points, from 0 A to 2 A with an increment of 0.1 A since our motor driver will be running less overall amperage than our SBC power supply. We also accounted for cable loss both ways in terms of input and output as well, giving us accurate measurements. Our efficiency here peaks at around 92% at around 0.15% of our max load. Here, instead of constant current running, it will spike depending on the distance, step size, and speed. Even at maximum load, we are able to run our motor driver at 82% efficiency, meeting our needs and helping us visualize our motor driver when it's running.

*C. Imaging Results*

In order to quantify the performance of our camera, we characterized the wavelength capture characteristics as well as the spatial resolution. The wavelength measurement is below.

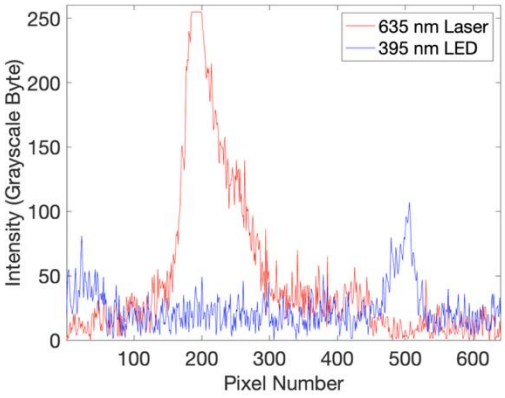


*Figure 14: Captured profiles of a 635 nm laser and 395 nm LED along one spatial pixel*

The scattered light of the translation stage while illuminated by a 635 nm laser and 395 nm LED was recorded. Using the peak values in this data, we get a pixel – to – wavelength conversion formula of

$$\lambda\,[nm] = 780.7 - 0.7668 * pix\# \qquad (4)$$

This current relation gives a wavelength of range of 491nm and a wavelength range of 290 nm – 781nm. The difference between this range and our target 350 nm – 900 nm is indicative of a lateral shift of the sensor on the order of 0.5 mm, which is consistent with the tolerances of 3D prints and fixable by slight modification of the camera housing.

A view of a portion of a ThorLabs R2L2S1N target is shown below. The native spatial axis (vertical in the figure) does reasonably well, resolving down to the 4.5

cycle/mm element. The scan was taken relatively fast at 0.85 mm/s and therefore the scan axis resolution (horizontal in the image) is not nearly as fine, struggling with the 1.0 cycle/mm target. This discrepancy can easily be solved by running a slower scan if the user desires.

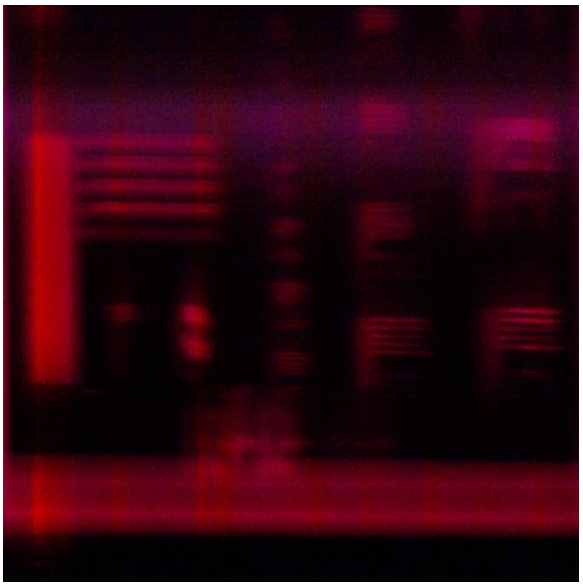

*Figure 15: Scanned image of ThorLabs R2L2S1N resolution target*

## IV. CONCLUSION

TSUNAMI will be able resolve important spectra that RGB cameras will not be able to. This project comprises of multiple optical and electrical systems combined to realize our goals and standards. We also tested and benchmarked multiple points that will help us explain the quantitative extent of our project. More extensive calibration and final touches will be added as we quickly near the end of our development.

## V. ACKNOWLEDGEMENT

The authors wish to acknowledge the assistance and support of BEAM Engineering for Advanced Measurements Co. (BEAM Co.) for providing funding for this project. Our budgetary allocation was paid for in full by our commercial sponsor, and without it this project would have been reduced in scope considerably.

## V. BIOGRAPHY

**Emilio Armas** is a dual major student between Photonics Science and Engineering, and Electrical Engineering. He intends to pursue an MSEE in electrical engineering under RF and Microwave design. He currently works for BEAM Co. as an electronics design engineer, and has experience in undergraduate research.

**Jacob Silver** is a Photonics Science and Engineering student at the University of Central Florida. His long-term career interests lie in infrared spectroscopy and lasing techniques, and he plans to pursue a PhD in Science at the University of Sydney under Dr. Benjamin Eggleton focusing on Brillouin interactions in the mid-infrared.

**Xander Kin** is an Electrical Engineering student at the University of Central Florida. His long-term careers interests are in RF design and specializing in RFIC. He plans to pursue an MSEE at the University of Central Florida as well, while working at Qorvo as a Reliability Engineer.

## VII. REFERENCES

Thorpe, A.K., Roberts, D.A., Bradley, E.S., Funk, C.C., Dennison, P.E., Leifer

I. (2013). High resolution mapping of methane emissions from marine and terrestrial sources using a Cluster-Tuned Matched Filter technique and imaging spectrometry. Remote Sensing of Environment, 134, 305-318.

Thompson, D. R., J. W. Boardman, M. L. Eastwood, R. O. Green (2017), A

Large airborne survey of Earth's visible-infrared spectral dimensionality. Optics Express 25, 9186-9195 (2017).

Moorhouse, J. (2020), Construction of a Hyperspectral Imager using

3D-printed and off-the-shelf components. University of Arkansas, Fayetteville

Hecht, Eugene, and Alfred Zając. *Optics*. pp 99–194. Addison-Wesley, 1974.